This manuscript is a non-peer reviewed EarthArXiv preprint. It is under review in *Journal of Geophysical Research: Solid Earth*.

Rates of olivine grain growth during dynamic recrystallization and post-deformation annealing

P.A. Speciale[1*], W.M. Behr[1,2], G. Hirth[3], and L. Tokle[2,3]

[1]Department of Geological Sciences, Jackson School of Geosciences, The University of Texas at Austin, Austin, Texas, USA. [2]Geological Institute, Department of Earth Sciences, ETH Zürich (Swizz Federal Institute of Technology), Zürich, Switzerland. [3]Department of Earth, Environmental, and Planetary Sciences, Brown University, Providence, Rhode Island, USA.

Corresponding author: Pamela Speciale (pamela.speciale@utexas.edu)

Whitney Behr (wbehr@ethz.ch)

Key Points:

- Post-deformation grain growth of moderately wet olivine is slower than predicted by the previously published wet olivine grain growth law
- Grain boundary migration driven by gradients in strain energy density may delay the onset of grain growth driven by interfacial energy
- Grain size reduction by dynamic recrystallization can play an important role in the longevity of strain localization in Earth's lithosphere

This manuscript is a non-peer reviewed EarthArXiv preprint. It is under review in *Journal of Geophysical Research: Solid Earth*.

Abstract

We performed deformation and grain growth experiments on natural olivine aggregates with moderate olivine water contents (C_{OH} = 600±300 ppm H/Si) at 1000-1200°C and a confining pressure of 1400±100 MPa. Our experiments differ from published grain growth studies in that most were: 1) conducted on natural olivine cores rather than hot-pressed aggregates, and 2) dynamically recrystallized prior to or during grain growth. We combine our results with similar experiments performed by van der Wal (1993) at 1200-1300°C and fit the data to a grain growth relationship, yielding a growth exponent (p) of 3.2, activation energy (E_G) ~620±145 kJ/mol (~570±145 kJ/mol when accounting for the role of temperature on water content), activation volume (V_G) ~5x10^{-6} m^3/mol, and rate constant (k_0) of 1.8x10^3 m^{p}s^{-1}. Our E_G is within uncertainty of that predicted for dislocation creep of wet olivine (E^* = 480±40 kJ/mol). In samples that underwent a reduction in strain rate, grain size adjusted to the piezometer within 1.3-7.9% strain, suggesting the strain required to attain stress-grain size equilibrium is small for modest changes in stress. The active grain boundary migration processes during deformation and dynamic recrystallization affect the kinetics of post-deformation grain growth, as grain boundary migration driven by strain energy density (ρGBM) may delay the onset of grain growth driven by interfacial energy (γGBM). We compared our post-deformation grain growth rates with data from previously published hydrostatic annealing experiments on synthetic olivine. At geologic timescales, the growth rates are slower than predicted by the existing wet olivine grain growth law.

1 Introduction

The rate of olivine grain growth has important implications for the viscosity (Freed et al., 2012; Hirth & Kohlstedt, 1996), seismic properties (Faul & Jackson, 2005; Jackson et al., 2002), chemical reactivity (Rubie, 1983; White et al., 1980), melt transport (King et al., 2010; Zhu et al., 2011), and persistence of plate boundary shear zones within Earth's mantle (Bercovici & Ricard, 2012; Korenaga, 2013). Small grain sizes, for example, promote linear-viscous grain size-sensitive creep, whereas grain growth commonly facilitates a transition to power-law viscous creep with weak to no grain size dependence (e.g., Chopra & Paterson, 1984; Hirth & Kohlstedt, 1995; Karato et al., 1986; Mei & Kohlstedt, 2000). Small grain sizes can also enhance chemical reactions due to increased surface area and can promote strain localization or 'reaction softening' through the nucleation of weak new phases (e.g., Newman et al., 1999; Newman & Drury, 2010; White & Knipe, 1978). Furthermore, large-scale geodynamic models that incorporate parameters for rheological 'damage' (grain size reduction) and 'healing' (grain growth) mechanisms are most successful at reproducing self-consistent plate-like behavior on Earth and other terrestrial planets (e.g., Bercovici & Ricard, 2014; Foley et al., 2012; Rozel et al., 2011).

An important aspect of olivine grain growth is its role in balancing grain size reduction processes during dynamic recrystallization. An olivine aggregate deforming in the dislocation creep regime will dynamically recrystallize to a grain size characteristic of the flow stress (Karato et al., 1980; van der Wal et al., 1993). These newly recrystallized grains can enhance deformation by grain size-sensitive creep (e.g., diffusion creep) at a lower stress, which can lead to weakening and strain localization (Poirier, 1980). Some researchers argue, however, that persistent strain localization resulting from dynamic recrystallization is improbable because of a dynamic balance between grain size reduction and grain growth (e.g., De Bresser et al., 2001).

This idea is supported by the paleowattmeter of Austin and Evans (2007; 2009), who proposed that grain size evolution is controlled by the rate of mechanical work ($\sigma\dot{\varepsilon}$) during deformation, and that a stabilized grain size distribution is established when grain growth and grain size reduction rates are balanced. The paleowattmeter accurately predicts recrystallized grain sizes in experimentally deformed quartz (Kidder et al., 2016; Stipp & Tullis, 2003), calcite (Barnhoorn et al., 2004; Rutter, 1995; Schmid et al., 1980), and olivine (Karato et al., 1980; van der Wal et al., 1993). If grain growth keeps pace with grain size reduction, strain localization may be less prominent, and may be temporary or episodic if the grains are refined and grow in cycles (Drury et al., 1991; Handy, 1989). If grain growth is slow, however, the maintenance of small grain size could enable prolonged localization (Platt & Behr, 2011). Thus, quantifying the rate of olivine grain growth during deformation is essential to our understanding of the persistence of strain localization in the upper mantle and the fossilization potential of ancient plate boundaries.

Existing olivine grain growth laws are quantified based on annealing experiments on synthetic aggregates under a limited range of conditions (e.g., Faul & Scott, 2006; Karato, 1989; Nichols & Mackwell, 1991; Ohuchi & Nakamura, 2007). Faster growth rates are reported for water-saturated olivine annealed at 1200-1300°C and 300 MPa confining pressure (Karato, 1989). Significantly slower growth is predicted for dry Forsterite sol-gel at 1200°C and 1200 MPa confining pressure (Ohuchi & Nakamura, 2007). Few experimental grain growth studies have been conducted on dynamically recrystallized olivine aggregates (e.g., doctoral dissertation of van der Wal, 1993), so the potential influence of stored strain energy on subsequent annealing is not well understood. In this study, we compare syn- and post-deformation grain growth of natural olivine aggregates with moderate olivine water content (C_{OH} = 600 ± 300 ppm H/Si) with static grain growth of water-saturated synthetic olivine (Karato, 1989) to investigate how microstructurally stored strain energy influences grain growth of dynamically recrystallized olivine. We quantify the growth rate of the recrystallized grains, qualitatively assess grain boundary migration processes, and discuss the implications for grain size evolution in upper mantle shear zones.

2 Experimental Methods

2.1. Starting Materials

Experiments were conducted on samples cored *as-is* from a single block of Balsam Gap dunite, a natural olivine aggregate with a weak pre-existing crystallographic preferred orientation (CPO). The average grain size is ~400 μm; however, larger grains (2-5 mm) are observed in some samples. The dunite is composed of ~99 vol% olivine (Fo_{92}) and ~1 vol% chromium spinel, with homogeneous chemical composition. The olivine exhibits an annealed texture with minor undulose extinction and straight to gently curved grain boundaries that commonly form ~120° triple junctions (Figure 1a).

Olivine hydroxyl concentrations were measured in grains from the starting material (C_{OH} ~350 ppm H/Si) and a deformed sample (C_{OH} ~900 ppm H/Si) using Fourier transform infrared (FTIR) spectroscopy at The University of Texas at Austin. We applied the calibration of Paterson (1982) using the parameters of Kohlstedt et al. (1996) (see supporting information S1 for details). The FTIR spectra in the starting material have sharp peaks at 3572 and 3523 cm^{-1} that are associated with structural water in olivine (e.g., Kohlstedt et al., 1996). However, the spectra are broad in the deformed sample (w2018). The reason for this is unclear, but we

speculate that that beam may have encountered subgrain boundaries. Because of the large uncertainties in our measurements, we use C_{OH} = 600 ± 300 ppm H/Si to bracket the range of measured olivine water content. Chlorite, talc and serpentine have been reported in dunites from Balsam Gap (e.g., Hunter, 1941). Although these hydrous phases were not observed in the samples selected for the experiments, dehydration of a very small amount of alteration phases along microcracks or grain boundaries may have elevated the water content during our high-temperature deformation experiments. For example, serpentine contains ~14 wt% H_2O; dehydration of just 0.014 vol% serpentine would produce ~20 wt ppm H_2O (equivalent to about 320 ppm H/Si in olivine), and such a small volume fraction would be hard to detect. We determined weight loss (approximately 0.4 wt%) upon drying cores of the dunite starting material in a controlled atmosphere furnace at 1000°C for 10 hours ($CO:CO_2$ = 1:5). Thus, there is enough additional water in the starting material (present along grain boundaries, fluid inclusions and trace alteration phases) to explain the modest increase in water content for the deformed samples.

2.2. Sample Assembly

The sample assembly is shown in Figure 1b. Cylinders (5 mm diameter) were cut to a length of ~13 mm and the ends were ground parallel. Each core was mechanically sealed in an inner Ni and outer Pt jacket, with Ni and Pt end discs, and surrounded by an additional thin Ni sleeve that extended ~3 mm beyond the alumina deformation pistons. Temperature was measured with a type-S (Pt-Pt10%Rh) thermocouple seated outside the Ni sleeve at the sample center. A molten salt cell composed of a eutectic mixture of NaCl-KCl was used as the confining medium inside the graphite furnace; solid NaCl was used outside the furnace.

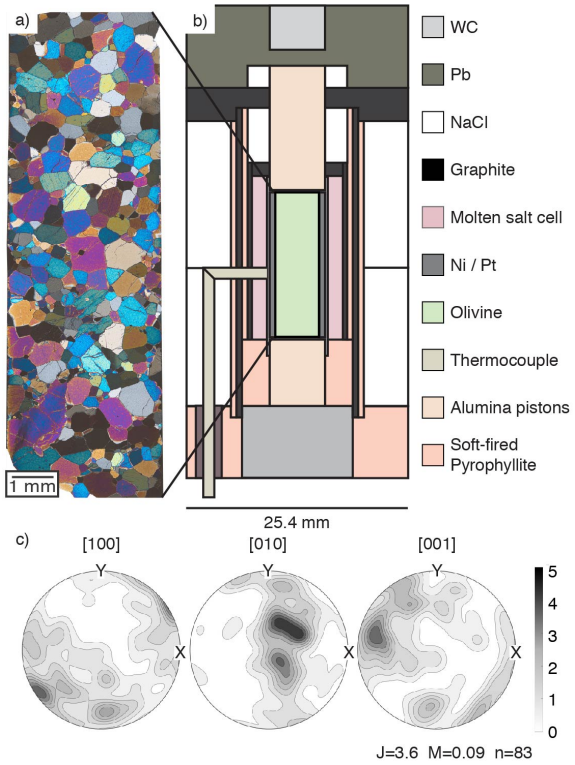

Figure 1. Starting material and sample assembly. a) Cross-polarized micrograph of Balsam Gap dunite core prior to experimentation, as inset to b) schematic diagram of molten salt assembly. c) Lower hemisphere, equal area pole figures of CPO observed in the starting material, constructed from electron backscatter diffraction (EBSD) data. A de la Vallee Poussin half width of 10° was used to generate pole figures in MTEX 5.1.1; the *J* index, *M* index, and number of grains *n* are shown. The deformation axis is vertical; we did not keep track of the initial orientation of the X and Z axes of the cores in the samples used for deformation experiments.

2.3. Experimental Procedures

Three types of deformation experiments were conducted to investigate the rate of grain size evolution during and after deformation (Table 1): 1) constant strain rate ($1.5x10^{-4}$ or $1.5x10^{-5}$ s^{-1}); 2) strain rate stepping, by decreasing the strain rate from either $1.5x10^{-4}$ or $1.5x10^{-5}$ s^{-1} to $1.5x10^{-6}$ s^{-1}; and 3) post-deformation stress relaxation, accomplished by stopping the advancement of the deformation piston. Samples were deformed in axial compression in a Griggs-type apparatus at 1000-1200 ± 5°C and 1400 ± 100 MPa confining pressure. Temperature and pressure were incrementally raised to experimental conditions over ~8 hours and maintained for an additional hour before advancing the deformation piston. Total engineering strain magnitudes up to 38% were obtained at constant displacement rates equivalent to axial strain rates of $1.5x10^{-4}$ to $1.5x10^{-6}$ s^{-1}. Upon achieving ~30% strain, samples were either quenched or grain growth intervals were initiated through either post-deformation stress relaxation or continued deformation at a slower strain rate ($1.5x10^{-6}$ s^{-1}) for various time increments. The goal of these experiments was to investigate the evolution of grain size upon a change in strain rate, thus in some cases (i.e., after a short amount of time after the change to a lower strain rate) a new steady state flow stress was not achieved.

To facilitate comparison to previous work on grain growth during static annealing, a hydrostatic grain growth experiment was performed on hot-pressed powders of Balsam Gap dunite and San Carlos olivine that were ground separately in an agate mortar and sieved to a particle size of 10-20 μm. The powders were positioned at the axial position of the thermocouple, separated by Pt discs, bounded by two Balsam Gap dunite cylinders (above and below), and annealed for ~25 hours at 1100°C. The initial grain size (7-8 μm) of these hydrostatic experiments was constrained by conducting an experiment in which the sample was held at 1000°C for 10 minutes.

Experiments were terminated by lowering the temperature (~2.2°C s^{-1}) to 300°C to preserve the microstructures, then maintaining the differential stress between 100-200 MPa as the remaining temperature and confining pressure were slowly (4-6 hours) lowered to room conditions to suppress decompression cracking. After quenching, samples were cut longitudinally and impregnated with epoxy, and one half was used for thin sectioning.

2.4. Analytical Procedures

Axial force, axial displacement, confining pressure and temperature were recorded at 1 Hz. Axial force was measured with an external load cell in line with the axial column, and axial displacement was measured with a DCDT (Tullis & Tullis, 1986). Load values (σ_1) were corrected for the piston friction, which we assume is constant for a given displacement rate (Proctor & Hirth, 2015). We also assume a constant sample volume over the duration of our experiments. Axial stress and axial strain were calculated using methods outlined in the RIG program (https://sites.google.com/site/rigprogram/file-cabinet), which accounts for rig stiffness and changes in confining pressure.

As illustrated below, the observed relationship between flow stress and recrystallized grain size for samples deformed at constant strain rate was consistently within the uncertainty of the olivine grain size piezometer (van der Wal et al., 1993). Thus, the piezometer was used to estimate the recrystallized grain size at the beginning of the grain growth intervals (d_0) in rate-stepping and stress relaxation experiments, using the final stress of the preceding deformation interval (Table 1). Due to the limited amount of recrystallization (5-10%) in each sample, the grain sizes of porphyroclasts were similar to that before deformation (~400 μm). Recrystallized grains were thus easily distinguished from porphyroclasts by their ~order of magnitude smaller size (~2-36 μm). The recrystallized grains occurred in patches around porphyroclast grain boundaries, and most were surrounded by other recrystallized grains of similar size. The recrystallized grain size was measured in regions near the axial position of the thermocouple to avoid effects of thermal gradients in the samples; however, the grain sizes throughout the samples were similar. Measurements were made in cross-polarized light in thin section (~15 μm-thick) with Zeiss Zen Pro software connected to a Zeiss Axio Imager M2m petrographic microscope. To analyze recrystallized grain sizes at the end of each experiment (d_f), we measured the length of a line across the intermediate axis (representing the average of the long and short axes) of each grain, applied a geometric correction factor of 1.75 (following van der Wal, 1993), and recorded the geometric mean of the distribution for each sample (Table 1; see supporting information Figure S2 for histograms). For several samples, grain size measurements were also made using two other complementary methods: 1) for three samples we used the mean linear intercept method on crossed-polarized micrographs, and 2) we used the equivalent circle

diameter on EBSD maps. Grain sizes measured using all three methods were the same within error.

EBSD maps used to analyze microstructural characteristics were acquired with a Philips/FEI XL30 environmental scanning electron microscope at The University of Texas at Austin, using a 20 kV accelerating voltage, ~16-mm working distance, and ~0.5-2.0 μm step size. Data were collected using Oxford AZtec software (version 2.1), and processed with MTEX 5.1.1 (Bachmann et al., 2010).

Expt #	T (°C)	Peak σ (MPa)	Flow σ (MPa)	Final σ (MPa)	Expt $\dot{\varepsilon}$ (s^{-1})	Strain rate step $\dot{\varepsilon}$ (s^{-1})	Deform Strain %	Growth Strain %	Total Strain %	Time (s)	d_0 (µm)	d_f (µm)	Std Dev	N (grains)
Constant Strain Rate														
w2015	1200	165	118	118	1.5×10^{-5}		28.3	--	28.3		26.3	34.5	7.8	260
w1990	1100	323	256	256	1.5×10^{-5}		29.9	--	29.9		9.4	10.0	2.2	302
w1969	1100	539	426	426	1.5×10^{-5}		27.7	--	27.7		4.8	5.1	1.2	334
w2091	1000	769	649	649	1.5×10^{-5}		25.9	--	25.9		2.7	2.3	0.3	115
w2090	1100	1076	782	782	1.5×10^{-4}		21.0	--	21.0		2.1	2.4	0.5	82
Strain Rate Stepping														
w2014	1200	204	191	96	1.5×10^{-5}	1.5×10^{-6}	30.9	4.8	35.8	32590	13.8	35.8	11.1	387
w2017	1200	294	254	138	1.5×10^{-5}	1.5×10^{-6}	28.0	1.3	29.3	5000	9.5	18.3	4.9	441
w2012	1100	461	461	300	1.5×10^{-5}	1.5×10^{-6}	28.9	0.3	29.2	540	4.3	6.2	1.9	291
w2003	1100	533	449	219	1.5×10^{-5}	1.5×10^{-6}	28.7	7.6	36.3	50030	4.4	10.9	2.9	354
w2076	1000	605	405	220	1.5×10^{-5}	1.5×10^{-6}	27.3	7.4	34.7	50320	5.1	8.0	1.6	84
w2002	1100	558	547	222	1.5×10^{-5}	1.5×10^{-6}	21.2	7.9	29.2	50040	3.4	11.2	2.6	498
w2069	1100	802	628	200	1.5×10^{-4}	1.5×10^{-6}	30.0	7.9	37.9	51030	2.9	10.8	2.7	332
Stress Relaxation														
w2018	1200	222	175	6	1.5×10^{-5}		28.6	0.3	28.9	5000	15.6	32.5	6.0	528
w1967	1100	321	213	97	1.5×10^{-5}		28.9	0.2	29.2	540	12.0	11.4	3.7	428
w1966	1100	346	285	46	1.5×10^{-5}		28.4	0.3	28.7	4960	8.2	10.2	3.1	485
w1964	1100	399	273	10	1.5×10^{-5}		29.4	0.5	29.8	50330	8.6	11.2	3.0	434
w2005	1100	377	333	0	1.5×10^{-5}		29.0	0.5	29.5	9950	6.6	10.1	2.7	322
w2086	1100	729	576	0	1.5×10^{-4}		26.8	0.5	27.3	27166	3.2	9.1	2.1	318
w2089	1100	872	472	4	1.5×10^{-4}		28.4	0.7	29.1	50010	4.2	9.7	2.2	464
Hydrostatic Annealing														
w2079BG	1000		--	--						600	--	8.0	3.9	300
w2079SC	1000		--	--						600	--	6.8	2.9	300
w2084BG	1100		--	--						88877	8.0	14.6	4.4	300
w2084SC	1100		--	--						88877	6.8	15.9	4.6	300

Table 1. Experimental conditions and results

This manuscript is a non-peer reviewed EarthArXiv preprint. It is under review in *Journal of Geophysical Research: Solid Earth*.

3 Results

3.1. Stress vs. Axial Strain

Differential stress vs. axial strain curves are plotted in Figure 2. At a given condition, the stress varied somewhat between experiments, likely as a result of heterogeneous water content from dehydration of minor hydrous phases and/or the presence of large porphyroclasts. The associated variation of the recrystallized grain size for these samples (Figure 3a), which follows the piezometer of van der Wal et al. (1993), enabled investigation of post-deformation grain growth over a range of starting grain sizes. In experiments that achieved flow stresses greater than ~600 MPa, significant strain weakening was observed following the peak stress; weakening in lower stress experiments was less pronounced. Constant strain rate experiments were quenched without a grain growth interval (Figure 2a). In rate-stepping experiments, the flow stress adjusted to the reduced strain rate (Figure 2b). In the rate-stepping experiment that achieved the highest peak stress (w2069), the stress dropped significantly after the strain rate was reduced then gradually increased during continued deformation, eventually achieving a final stress similar to that observed in other rate-stepping experiments at the same temperature. In all stress relaxation experiments, the flow stress decreased rapidly when advancement of the deformation piston was stopped, and accumulation of additional strain was less than 1% (Figure 2c).

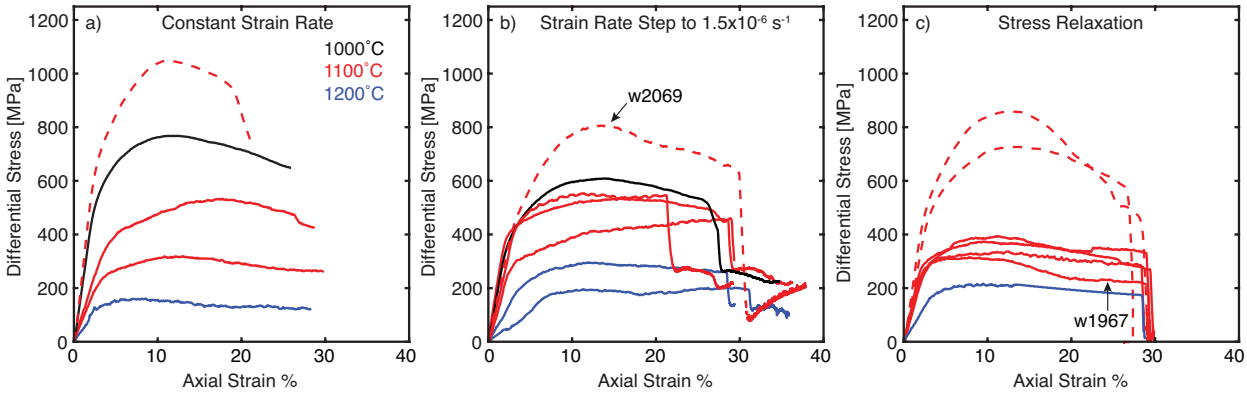

Figure 2. Differential stress vs. axial strain. a) Constant strain rate experiments; b) strain rate stepping experiments, wherein the strain rate during deformation was either $1.5x10^{-5}$ s^{-1} (solid) or $1.5x10^{-4}$ s^{-1} (dashed) and was reduced to $1.5x10^{-6}$ s^{-1}; and c) stress relaxation experiments.

3.2. Stress vs. Grain Size

To illustrate the effect of stress reduction on grain growth of deformed (or deforming) olivine aggregates, the final stress magnitude and final grain size data are plotted for each experiment in Figure 3. Because the relationships between flow stress and grain size in constant strain rate experiments (Figure 3a) are consistently within the uncertainty of the olivine grain size piezometer (van der Wal et al., 1993), the piezometer was used to estimate the starting recrystallized grain size in the rate-stepping and stress relaxation experiments. For the rate-stepping experiments, lines connecting each final stress/grain size to the olivine piezometer indicate the flow stress just prior to the change in strain rate, and the calculated grain size at the

start of the grain growth interval (Figure 3b). In rate-stepping experiments, the stress drop was relatively modest (consistent with the dislocation creep flow law – see Section 3.3) and recrystallized grain sizes remained similar to those predicted by the piezometer. In contrast, grain sizes in samples that underwent stress relaxation, wherein stress drops were significantly larger, no longer followed the piezometer (Figure 3c). The final grain size (11.4 µm ± 3.7 µm) in the sample with the shortest relaxation interval (w1967; 540 seconds) is smaller than, but within uncertainty of, the initial grain size (12 µm) predicted for its flow stress (213 MPa). Data from stress relaxation experiments conducted on the Anita Bay and Åheim dunites at 1200-1300°C (van der Wal, 1993) are also shown. The grain size evolution observed for van der Wal's samples is similar to that we observe for Balsam Gap dunite.

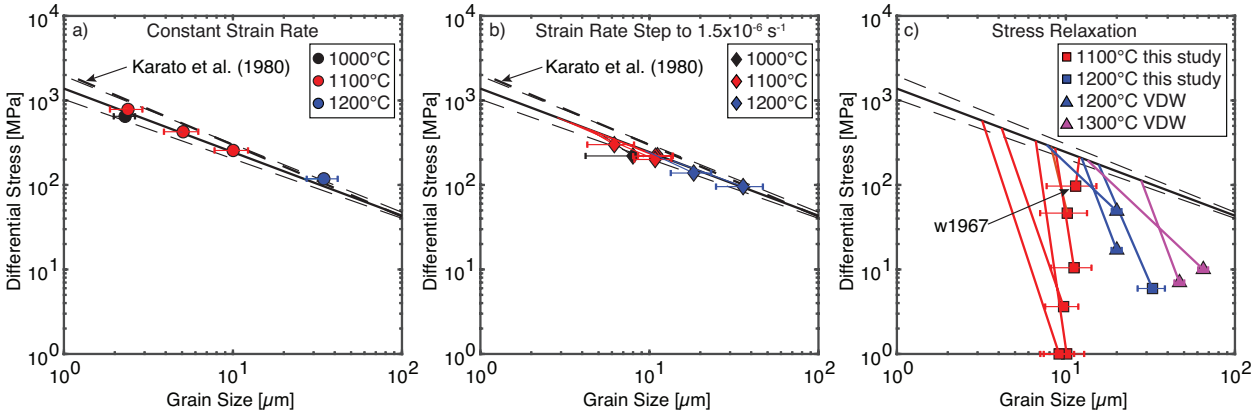

Figure 3. Stress-grain size relationships for each type of deformation experiment. The solid line is the olivine piezometer; light dashed lines represent the uncertainty in the piezometer (van der Wal et al., 1993). The olivine piezometer of Karato et al. (1980) is plotted for comparison (heavy dashed line in Figures 3a and 3b). Error bars represent one standard deviation of the grain size distribution. Data from stress relaxation experiments by van der Wal (1993) are also shown.

3.3. Strain Rate vs. Stress

Strain rate vs. differential stress relationships are plotted using the wet olivine flow law for dislocation creep (Hirth & Kohlstedt, 2003) at water contents of C_{OH} = 600 ± 300 ppm H/Si (Figure 4). The final stress and strain rate for constant strain rate experiments are plotted in Figure 4a. The data from rate-stepping experiments give "two-point" stress exponents (n) from 2.6 to 4, consistent with deformation by dislocation creep, although most samples from rate-stepping experiments deformed at somewhat higher stresses than predicted by the flow law (Figure 4b). The higher stress exponent for sample w2012 (n = 5) reflects the short duration of deformation after the step (540 seconds) during which steady stress was not achieved before quenching. The stress in the sample deformed at 1000°C (w2076) is significantly lower than predicted by the flow law, which could be related to higher water content. Nonetheless, the recrystallized grain size data for w2076 agree with the recorded flow stress. For the stress relaxation experiments, the strain rate and stress data (prior to relaxation) agree reasonably well with the dislocation creep flow law for this range of water contents (Figure 4c).

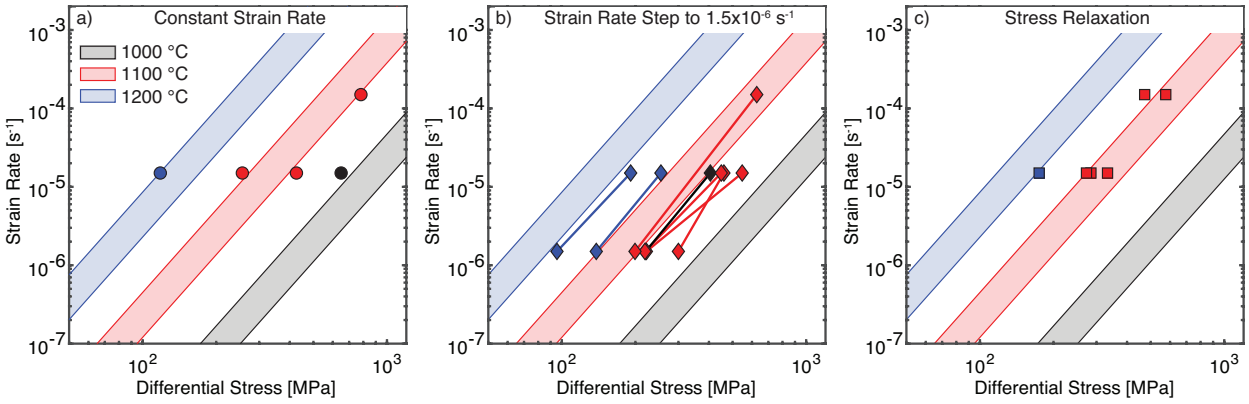

Figure 4. Comparison of the flow law for wet dislocation creep to our observed strain rate vs. differential stress data. The colors of the data points represent the temperature for each sample. In b), solid lines connect the final stress of the initial deformation interval to the final (lower) stress after the strain rate step. Shaded regions represent the range of stress-strain rate relationships predicted by the flow law for each temperature over the range of measured water contents (C_{OH} = 300-900 ppm H/Si).

3.4. Microstructural Observations

3.4.1. Thin section-scale

To confirm that no significant grain growth occurred during hot-pressing of this coarse-grained aggregate, we performed a "null" experiment, wherein a dunite core was taken to 1100°C and a confining pressure of 1400 MPa and held for ~10 hours. As expected, no significant grain growth occurred; the grain size distribution remained similar to that in samples used in the other experiments (~400 μm). Cross-polarized micrographs of the samples are shown in Figure 5. Deformation resulted in variable degrees of grain flattening perpendicular to the direction of maximum principal compressive stress (σ_1, vertical), and dynamic recrystallization along porphyroclast grain boundaries. Because of the relatively low strain magnitudes and small recrystallized grain size, none of the samples achieved complete recrystallization. The degree of dynamic recrystallization was generally 5-10%, although some higher temperature experiments (e.g., w2018) exhibit up to ~30% recrystallization. Several samples exhibit relatively uniform shortening. Others appear somewhat bent, likely due to the presence of large porphyroclasts, as most of the samples with large porphyroclasts bent to some degree. Deformation of one sample (w2089, with a peak stress of 872 MPa) resulted in a brittle fracture oriented ~30° to σ_1; however, brittle behavior occurred subsequent to dynamic recrystallization, enabling evaluation of grain growth during stress relaxation. Although no brittle behavior is observed in sample w2090 (with a peak stress of 1076 MPa), the sample exhibits kink bands and only minor recrystallization.

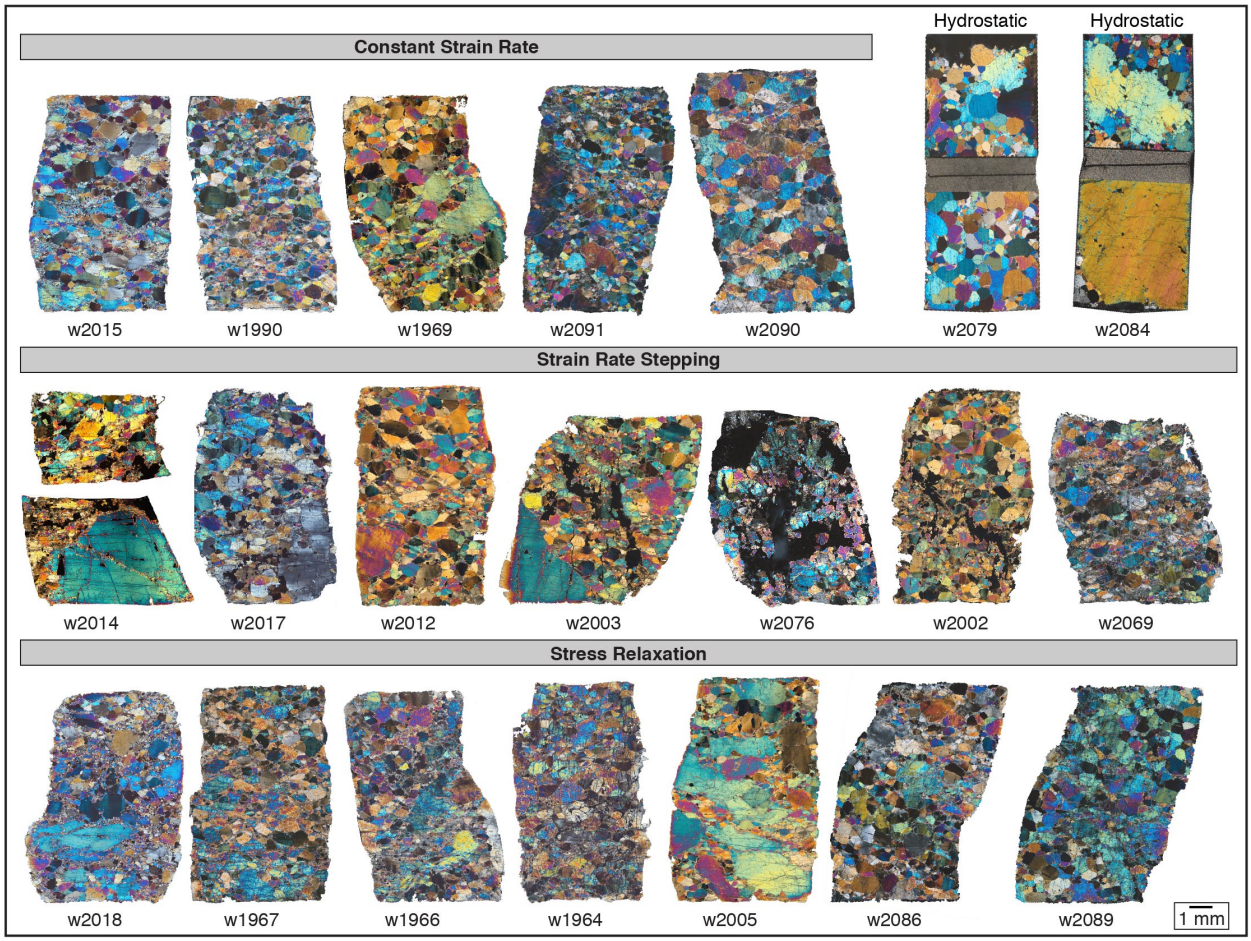

Figure 5. Thin section-scale micrographs organized by experiment type with increasing flow stress from left to right. The top-right images are the hydrostatic experiments on hot-pressed Balsam Gap dunite and San Carlos olivine powder (sample center) bounded above and below by Balsam Gap dunite cylinders; all others are deformed Balsam Gap dunite cores. Sample w2014 broke in half upon removal from the assembly. Much of the recrystallized regions in w2076 were plucked during thin sectioning, thus the grain size measurements were limited.

3.4.2. Grain-scale

Representative cross-polarized micrographs are shown in Figure 6. Dynamically recrystallized grains are much smaller than the porphyroclasts. Some recrystallized grains are approximately equant; others are somewhat flattened, with aspect ratios up to 3:1. Grain boundaries in samples quenched after deformation at a constant strain rate are lobate and/or sutured (Figure 6a), but regions with straight to gently curved grain boundaries are also observed in EBSD band contrast maps of the same sample (Figure 6b). The intracrystalline deformation textures of samples from rate-stepping experiments (in all of which the strain rate was decreased to 1.5×10^{-6} s^{-1}) are similar to that observed in samples from constant strain rate experiments (Figures 6c and 6d). Samples from stress relaxation experiments have straight to gently curved grain boundaries and ~120° triple junctions, and recrystallized grains exhibit a lesser degree of undulose extinction than that observed in samples from constant strain rate and rate-stepping

experiments (Figures 6e and 6f). In addition, larger recrystallized grains in the stress relaxation samples tend to have more than six sides and are convex inward on at least one boundary, adjacent to smaller convex-out grains with fewer grain boundaries, indicating grain boundary migration driven by the reduction of grain boundary curvature (Atkinson, 1988).

The original deformation microstructures are overprinted during changing conditions in stress relaxation and rate-stepping experiments; however, the original recrystallization mechanism may be inferred from analysis of the constant strain rate experiments. Grain size in samples deformed at lower stress (<400 MPa) is similar to subgrain size, suggesting that subgrain rotation played a role in recrystallization (Figure 6a). However, bulging and sutured grain boundaries indicate that gradients in strain energy density also promoted bulge nucleation. Subgrains are less prominent in samples that deformed at higher stress (>400 MPa), and recrystallization is less abundant. In the highest stress samples (>700 MPa), very little recrystallization is observed, and microstructures are characterized by kink bands and/or indicative of brittle behavior.

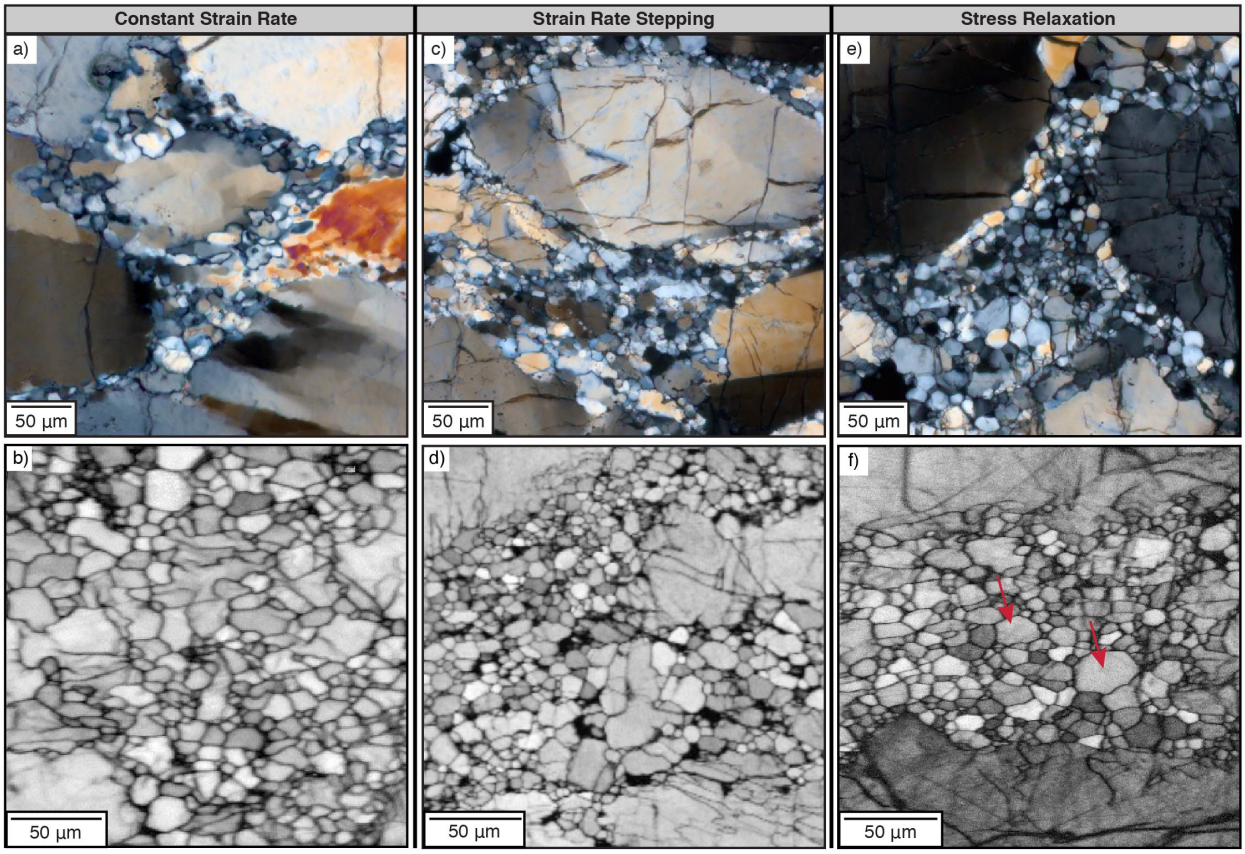

Figure 6. Representative cross-polarized micrographs for each type of experiment, and EBSD band contrast maps of different regions within the same samples. a and b) Constant strain rate (w1990, peak stress = 323 MPa), c and d) rate-stepping (w2002, 558 MPa), e and f) stress relaxation (w1964, 399 MPa); larger grains are convex inward adjacent to smaller grains (red arrows in f). Dark regions are plucked grains. Shortening direction is vertical.

3.4.3 Microstructures of Hot-pressed, Annealed Olivine Aggregates

The hot-pressed Balsam Gap dunite and San Carlos olivine aggregate (w2084BG and w2084SC, respectively) have relatively uniform grain sizes, and straight to gently curved grain boundaries that form ~120° triple junctions (Figure 7). Larger grains tend to be convex inward on at least one boundary and smaller adjacent grains are convex out, consistent with expectations for grain growth. Because this sample was hot-pressed and annealed at a confining pressure of 1400 MPa, we infer that only a small amount of porosity remains (<1 vol%); similarly, no porosity was observed in the recrystallized regions of the deformed specimens of coarse-grained cores. The grain boundary morphologies of our hot-pressed annealed sample are similar to those from stress relaxation samples, but they differ somewhat from the microstructures of constant strain rate and rate-stepping samples that still exhibit evidence of deformation, such as sutured grain boundaries and undulose extinction.

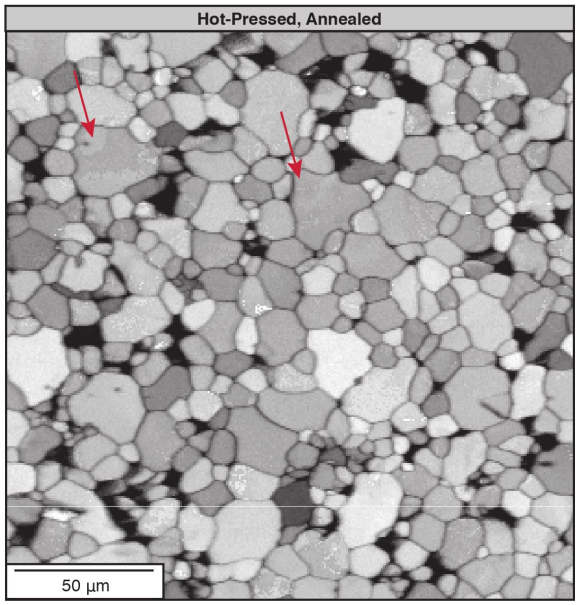

Figure 7. EBSD band contrast map of hot-pressed annealed Balsam Gap dunite (w2084BG). Larger grains tend to have more than six sides and are convex inward on at least one boundary, adjacent to convex-out grains with fewer grain boundaries (red arrows). Dark regions are plucked grains.

3.5. Dislocation Density Estimation

Dislocation density (ρ) maps of representative samples were constructed from EBSD data using the Dislocation Density Estimation routine in MTEX 5.1.1 (Figure 8), which is based on the method of Pantleon (2008). Warmer and cooler colors indicate higher and lower ρ, respectively. The color bars represent the log10 ρ (m^{-2}) of geometrically necessary edge and screw dislocations that are required to accommodate the intragranular misorientations; the step sizes used to acquire each map are indicated. We used a step size of ≤ 1 µm for most of the maps; although a few maps were acquired at relatively low resolution (2 µm step size), we were still able to use them to make several key qualitative observations. We acknowledge that significant uncertainties arise from the use of lower-resolution EBSD techniques; however, our

qualitative comparisons between samples deformed under different conditions of stress and temperature are consistent with expectations for relative differences in ρ between highly deformed porphyroclasts and recrystallized grains.

The non-annealed, hot-pressed sample (w2079BG) has a relatively high ρ, suggesting that dislocations are generated during hot-pressing of the initial high-porosity material (Figure 8a); ρ was significantly lower (i.e., likely reduced) during annealing (w2084BG, Figure 8b). Samples that were deformed and then relaxed at 1100°C exhibit a reduction in ρ with increased annealing time (Figures 8c and 8d). In a few samples, the grain morphologies of some (often larger) recrystallized grains near the boundaries of porphyroclasts indicate growth preferentially in the direction of high ρ in the porphyroclasts (Figures 8e and 8f, arrows). In contrast, recrystallized grains that are surrounded by other recrystallized grains with similar dislocation density are similar in size. In sample w2015, which was deformed at a constant strain rate at 1200°C (Figure 8g), the recrystallized grains have a higher and more homogeneous ρ than the recrystallized grains in the sample that underwent stress relaxation at 1200°C (w2018, Figure 8h).

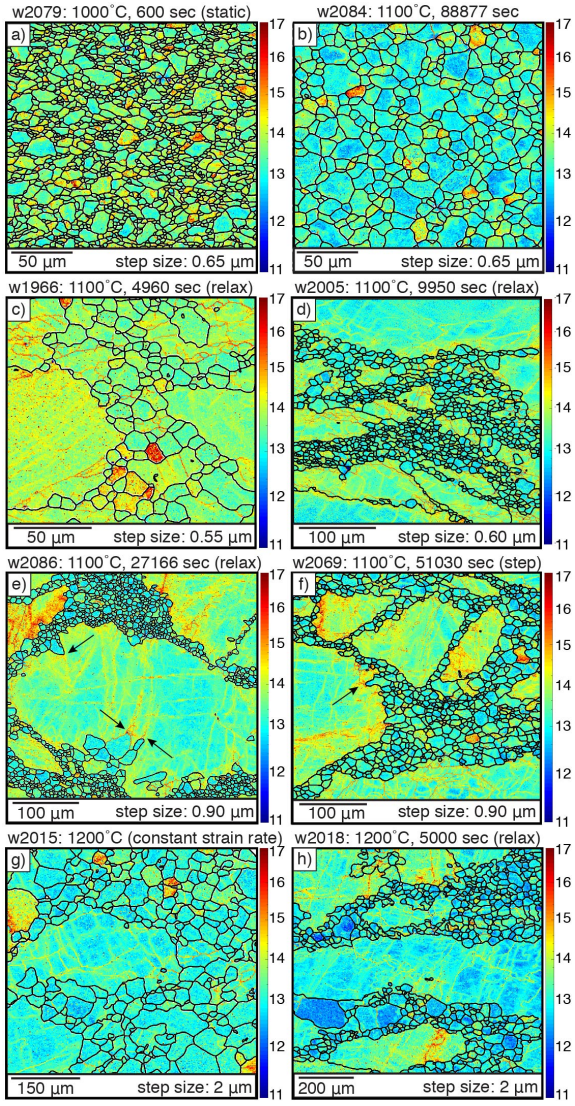

Figure 8. Dislocation density maps of representative samples, with EBSD step size indicated. The color bars represent $\log_{10} \rho$ (m^{-2}). In e) and f), arrows point to recrystallized grains that indicate growth in the direction of high ρ in the porphyroclast.

4 Discussion

4.1. Variability in Flow Stress

The variation in flow stress among experiments in this study enabled investigation of syn- and post-deformation grain growth for a range of starting grain sizes. Variation in stress magnitude may result from differences in temperature, starting material grain sizes and orientations, or water content.

4.1.1. Variation in Temperature

The temperature of each experiment was precise to within ±5°C at the position of the thermocouple; however, shifting of the thermocouple during deformation cannot be ruled out.

Although we measured recrystallized grain size at the axial position of the thermocouple (near the sample center), recrystallized grain sizes appeared similar throughout the sample. This suggests that variation in temperature within the sample was not large (current analyses of these gradients indicate that temperature varies less than 30°C in the axial direction, Eric Burdette, pers. comm., 2020).

4.1.2. Variation in Porphyroclast Size/Orientation

The size, distribution, and orientation of large porphyroclasts observed in several samples may affect the strength of the material. For example, among 1200°C experiments, the lowest flow stress (118 MPa) was recorded in a sample (w2015) that lacked large porphyroclasts, whereas the others had large porphyroclasts and were stronger (175-254 MPa). A similar correlation is observed in samples deformed at 1100°C. Although we observed a large porphyroclast and high stress in one sample deformed at 1000°C (w2091, 649 MPa), we are unable to determine if the lower stress in the other 1000°C sample (w2076, 405 MPa) may have been related to the absence of large porphyroclasts because large portions of material were plucked during thin sectioning.

4.1.3. Variation in Water Content

Although minor variations are to be expected in a natural aggregate, and cannot be avoided, the cores for each sample were very similar; thus, we infer that the starting water content of each sample was similar. The water source in our samples likely comes from dehydration of serpentine. Individual cores drilled from the block of *as-is* dunite may have sampled regions inside the rock with altered microcracks or grain boundaries that were not visible at the surface. The dehydration temperature of serpentine is well below the temperatures of our experiments; dehydration would have been accomplished fairly early along the path to 1100°C and 1400 MPa confining pressure, likely ~10 hours before deformation was initiated. Under these thermodynamic conditions, the saturated water content of olivine is ~2800 ppm H/Si (based on Zhao et al., 2004) with a water fugacity of ~4300 MPa (using Wither's fugacity calculator: http://www.esci.umn.edu/people/researchers/withe012/fugacity.htm); thus, the experiments were not performed under water-saturated conditions. However, three lines of evidence suggest that, whatever the water content, it had equilibrated reasonably well prior to the grain growth interval:

1) the similarity of stress magnitudes recorded in our samples that underwent stress relaxation at 1100°C following deformation at a strain rate of 1.5×10^{-5} s^{-1} (Figure 2c);
2) the consistency of the strain rate vs. stress data with the wet olivine flow law for our range of water contents (Figure 4c); and
3) the log-linear relationship in the change of grain size with time (see Section 4.2, Figure 9a).

These observations suggest that variation in water content did not affect the grain growth rates in the stress relaxation experiments we used to derive our grain growth law (see Section 4.2). In addition, the uncertainties we report in our grain growth parameters account for the uncertainties due to any variation in water content.

4.2. Grain Growth Kinetics of Deformed, Moderately Wet Olivine

The rate of post-deformation grain growth was analyzed using the stress relaxation experiments, assuming a normal grain growth relationship:

$$d_f^p - d_0^p = kt, \quad (1)$$

with grain size (d) in meters, a growth exponent (p), time (t) in seconds, and a growth rate (k) following the relationship:

$$k = k_0 * \exp\left(-\frac{H}{RT}\right), \quad (2)$$

where k_0 is the rate constant (m^p/s), H is the activation enthalpy (J/mol), R is the ideal gas constant (J/K/mol) and T is absolute temperature (Atkinson, 1988). Six of the stress relaxation experiments were conducted at a temperature of 1100°C; one (w1967) was not used because it had an apparent negative growth rate (i.e., its final grain size was slightly smaller than its starting grain size, although still within error). To estimate the growth rate (k) at 1100°C, we used least-squares polynomial fits to evaluate the change in grain size with time for grain growth exponents (p) ranging from 2 to 4. Errors are minimized for p = 3.2, although the errors for p = 3.3 were similar. The change of grain size with time is shown in Figure 9a, with associated residuals in Figure 9b. The goodness of fit for the each of the growth exponent values we evaluated is shown in Figure 10a. For the 1100°C experiments, a value of p = 3.2 results in a growth rate (k) of $2x10^{-21}$ $m^p s^{-1}$.

A grain growth exponent of p = 3 has been attributed to various rate-limiting growth mechanisms, such as impurity drag limited by lattice diffusion, and the effects of secondary phases (e.g., Brook, 1976). Our samples contain ~1 vol% chromium spinel and these grains are rare in regions of dynamically recrystallized olivine; thus, we interpret that second-phase pinning effects are minimized. An electron microprobe analysis of several samples suggests the CaO (<0.06 wt%) and Al_2O_3 (<0.15 wt%) concentrations are low (see supporting information, Figure S3); however, minor amounts of these incompatible components concentrated along grain boundaries may contribute to impurity drag and an exponent of p = 3.2 in our samples.

To calculate the parameters of the temperature-dependent growth rate (k), results from grain growth experiments at a range of temperatures are required. Because we only had one stress relaxation experiment at 1200°C, we incorporated the results of similar experiments performed by van der Wal (1993) on the Anita Bay and Åheim dunites (1200-1300°C, 300 MPa confining pressure) in our analysis (Figure 9c). The water content in samples used in van der Wal's experiments is similar to our samples (C_{OH} = 600 ppm H/Si; Behn et al., 2009). The growth rate (k) is an exponential relation, thus the activation enthalpy and rate constant may be obtained by taking the natural logarithm of both sides of Equation (2) to yield:

$$\mathrm{Ln}(K) = \left(-\frac{H}{R}\right) * \left(\frac{1}{T}\right) + \ln(k_0), \quad (3)$$

which gives an activation enthalpy of H = 622 kJ/mol, and a rate constant of $k_0 = 1.8x10^3$ $m^{3.2}s^{-1}$. The good agreement between growth rates determined during stress relaxation of dynamically recrystallized olivine (van der Wal, 1993; this study) suggests that confining pressure has only a minor effect on the growth rates at the pressures of these experiments (300 MPa and 1400 MPa,

respectively). To assess the effect of the pressure difference, we evaluated the components of the activation enthalpy (H), which is defined by the relationship:

$$H = E_G + P * V_G, \quad (4)$$

where E_G is the activation energy for grain growth (J/mol), P is the confining pressure (Pa), and V_G is the activation volume for growth (m^3/mol). Recognizing that, at the conditions of van der Wal's experiments, the pressure dependence of H is relatively small, we estimated E_G by testing V_G values in the range of $1x10^{-5}$ to $1x10^{-7}$ m^3/mol and found E_G = 619-622 kJ/mol at P = 300 MPa. We tested four values of E_G over this range of V_G and compared the predicted grain sizes with those from our stress relaxation experiments. Errors are minimized in the range of V_G = $4.6x10^{-6}$ to $6.7x10^{-6}$ m^3/mol. When we applied these values of E_G and V_G to both our results and van der Wal's data, the best fit was E_G ~620 ± 145 kJ/mol, where errors are minimized for V_G ~$5x10^{-6}$ m^3/mol (Figure 10b). We note that our activation energy for grain growth (E_G) is within uncertainty of the activation energy for dislocation creep of wet olivine (E^* = 480 ± 40 kJ/mol for constant water content; Hirth & Kohlstedt, 2003), acknowledging the relatively large uncertainty in our data. Accounting for the influence of temperature on the water content of olivine (with an activation energy of ~50 kJ/mol; Zhao et al., 2004), our estimate of E_G would be slightly lower (i.e., ~570 ± 145 kJ/mol).

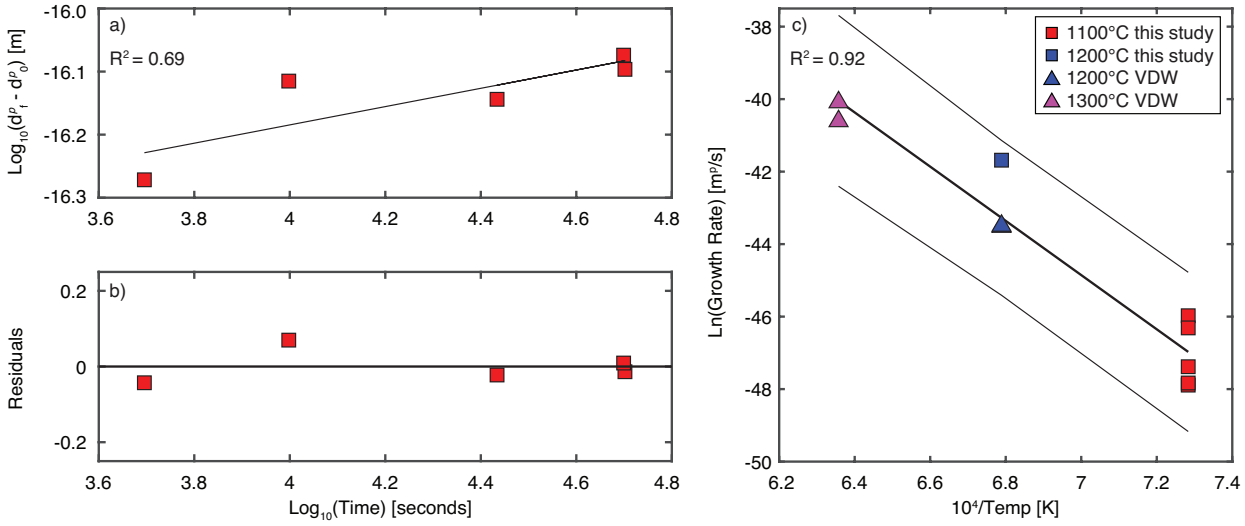

Figure 9. Parameterization of our grain growth equation. a) Change in grain size vs. time for 1100°C stress relaxation experiments, with p = 3.2; b) residuals vs. time: difference between experimentally determined values for data in a) and the best fit curve; and c) Arrhenius plot showing analysis to derive the activation enthalpy (H) and rate constant (k_0). Heavy line is the best fit curve; thin curves are 95% prediction bounds.

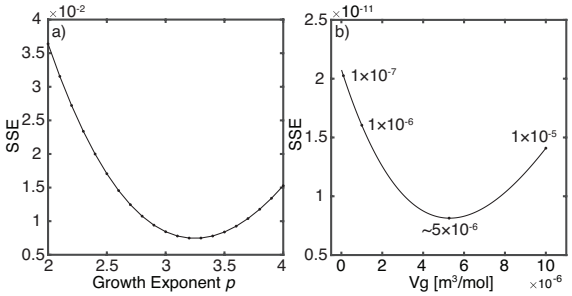

Figure 10. Goodness of fit for grain growth parameters. a) Sum of squared errors (SSE) for grain growth exponents ranging from 2 to 4, from analysis of change in grain size vs. time, and b) SSE for comparison of measured grain sizes to predictions using a range of activation volumes (V_G). Based on the data, errors are minimized for p = 3.2, E_G ~620 kJ/mol, and V_G ~5x10^{-6} m^3/mol.

4.3. Comparison of Static Annealing and Post-deformation Growth

4.3.1. Comparison to Our Olivine Grain Growth Parameters

Curves for predicted grain size evolution in our stress relaxation and rate-stepping samples, stress relaxation experiments by van der Wal (1993), and our hot-pressed annealed sample are plotted using Equation (1) along with final grain sizes in Figure 11a. Although data from the rate-stepping experiments are not included in the derivation of our parameters, they agree well with the stress relaxation experiments. Grain size in sample w2012 (6.2 ± 1.9 μm), for which the duration of the strain rate step was only 540 seconds, is within the uncertainty of the final grain size (7.6 μm) predicted for its final stress (300 MPa). All of the other samples from rate-stepping experiments at 1100°C record grain sizes (~10-11 μm) that are similar to those observed after stress relaxation experiments. These grain sizes are also similar to that predicted by the piezometer for the final stress observed during the step (~200 MPa), which would limit the grain sizes to these values. Grain size in a 1200°C rate-stepping sample (w2014) is larger than, but also within uncertainty of, the grain size predicted by our grain growth parameters. In the sample deformed and then relaxed at 1200°C (w2018), the grain size is also larger than predicted by our parameters.

Our grain growth parameters predict grain sizes that are smaller than, but within uncertainty of, the final grain sizes observed in our hot-pressed annealed sample (w2084) with Balsam Gap dunite and San Carlos olivine (stars, Figure 11a). Although the San Carlos olivine is dry, adsorbed water on the powder could result in a similar water content, and similar growth rates in both materials. Using a Pt disc (instead of Ni) to separate the hot-pressed aggregates may have impacted the oxygen fugacity, but the growth rates of the hot-pressed San Carlos and Balsam Gap dunite powders were very similar to each other and to that observed in the stress relaxation samples. At a confining pressure of 1400 MPa, densification was near-complete, thus most grain boundaries were in contact and growth may not have been significantly inhibited by porosity. This interpretation is supported by the similarity of growth rates at 1100°C of our hot-pressed annealed and stress relaxation samples in which no porosity was observed (and unlikely, since the recrystallized grains form by grain boundary migration and subgrain rotation from single crystal porphyroclasts). In the absence of deformation, we expected an initially low ρ and grain growth driven completely by the reduction of interfacial energy (γGBM) in the hot-pressed

annealed sample. γGBM acts to reduce boundary curvature, resulting in ~120° triple junctions (Humphreys & Hatherly, 1995). However, we observed relatively high ρ in the non-annealed sample (Figure 8a), which was higher than that observed after annealing (Figure 8b). Similarly, ρ is reduced with increased annealing time during stress relaxation (Figures 8c and 8d); ρ in the hot-pressed annealed sample (Figure 8b) is lower than that observed in the recrystallized grains of the stress relaxation sample with a relatively short annealing time (Figure 8c), but similar to that observed in the stress relaxation sample with a longer annealing time (Figure 8d). A difference in ρ across a grain boundary induces strain energy-driven grain boundary migration (ρGBM). Grains with lower ρ grow as their grain boundaries migrate into grains with higher ρ, which shrink in the process (Beck et al., 1950). If the distribution of dislocations is more homogeneous, however, grain boundaries will migrate randomly with little net change in the grain size distribution (Platt & Behr, 2011). The microstructures of the hot-pressed annealed and stress relaxation samples indicate that γGBM was dominant by the end of the experiment, but an interval of random ρGBM may have delayed the onset of γGBM or reduced its efficiency. Otherwise, it follows that γGBM itself leads to the observed grain growth rates.

In Figure 11b, we compare our grain growth parameters to the grain size data from previously published hydrostatic annealing experiments on hot-pressed olivine aggregates conducted under "wet" conditions at 1200-1300°C and a confining pressure of 300 MPa (Karato, 1989). The grain sizes plotted in Figure 11b have been normalized to account for the fact that Karato used a geometric correction factor of 1.5 (i.e., we removed his original correction factor by dividing by 1.5, then multiplied his grain sizes by 1.75). Although the grain sizes of a few of Karato's 1200°C samples are reasonably well predicted by our parameters, most are over-estimated; our parameters predict grain sizes significantly larger than observed for all of his 1300°C samples. As noted by Karato (1989), growth was inhibited by porosity in the samples used in his study. This could explain why the grain sizes in most of his samples are significantly smaller than predicted by our parameters, which are based on grain growth in samples wherein porosity was not observed.

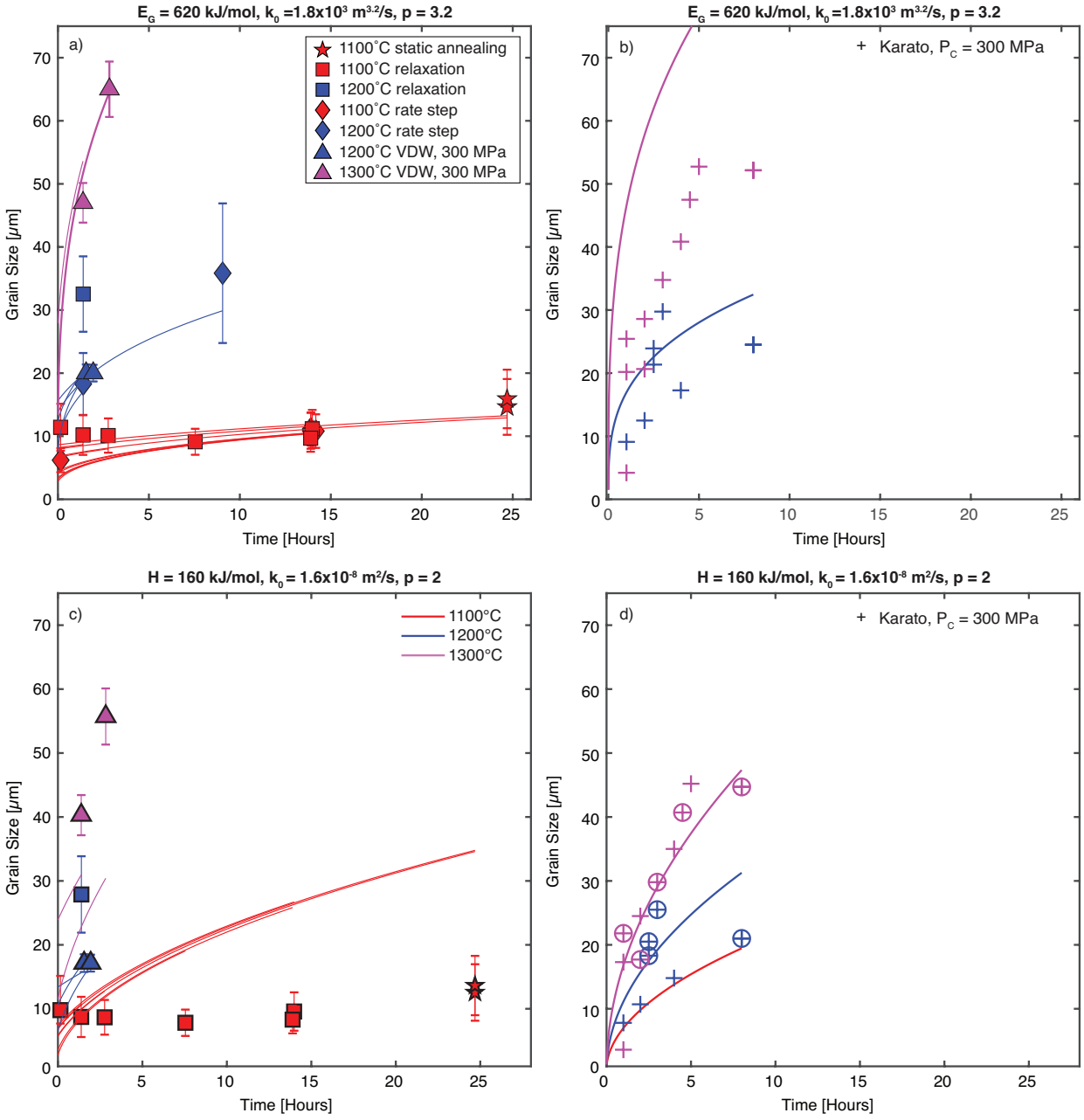

Figure 11. Comparison of olivine grain growth using the parameters of a-b) this study and c-d) Karato (1989), with growth curves plotted from the grain size at the start of the grain growth interval. The data points in each plot represent: a) final grain sizes from samples in this study (and relaxation experiments by van der Wal, 1993); b) normalized grain sizes from static annealing samples (Karato, 1989); c) same data as in a) but normalized to Karato's geometric correction factor of 1.5; and d) grain size data from Karato (1989). The circled crosses in d) indicate the samples Karato (1989) used to derive the grain growth law. Error bars in a) and c) represent one standard deviation of the grain size distribution. For data points and growth curves, temperature is indicated by colors in the legend in Figure 11c.

4.3.2. Comparison to the Existing Wet Olivine Grain Growth Law

We compare the grain sizes observed in our study (and van der Wal, 1993) with a grain growth law for wet olivine (Karato, 1989; with $p = 2$, $H = 160$ kJ/mol and $k_0 = 1.6\text{x}10^{-8}$ m^2s^{-1}) in Figure 11c. In this case to facilitate direct comparison to the grain growth law, the grain sizes plotted in Figure 11c are normalized using the geometric correction factor of 1.5 used by Karato (1989) (i.e., we removed our original correction factor by dividing by 1.75, then multiplied our grain sizes by 1.5). The Karato (1989) grain growth law is consistent with the grain sizes observed in van der Wal's samples that were deformed and then relaxed at 1200°C (blue triangles, Figure 11c). However, it over-estimates the grain sizes in both our hot-pressed annealed sample and the samples from our stress relaxation experiments conducted at 1100°C, and under-estimates the grain sizes from stress relaxation experiments at 1300°C (i.e., van der Wal, 1993). These observations are consistent with the difference between the activation enthalpy we determined and the lower value estimated by Karato (1989).

Curves for predicted grain growth at 1100-1300°C are plotted using the parameters of Karato (1989) in Figure 11d, along with the final grain size data of the wet samples in his study that were annealed at 1200-1300°C and a confining pressure of 300 MPa (crosses, Figure 11d). The data he used to derive the grain growth law are shown as circled crosses; we note that Karato (1989) did not perform annealing experiments at 1100°C. The initial grain size of his samples was ~1-4 μm. Because grain growth was inhibited by porosity in his samples, Karato only used samples with densities at least 97% of the theoretical density of olivine (3.33 g/cm^3) in his derivation. In addition, he performed progressive annealing experiments on two samples (one at 1200°C and one at 1300°C), wherein each sample underwent repeated annealing and quenching (to examine the grain size) over four sequential grain growth intervals; for these samples, only the final grain size data were used in the grain growth law (the two circled crosses plotted at $t = 8$ hours in Figure 11d). However, progressive annealing experiments can lead to water loss and can introduce porosity (due to repeated quenching/decompression) which may inhibit subsequent grain growth.

An important difference between the static grain growth experiments of Karato (1989) and the stress relaxation experiments in this study (and van der Wal, 1993) is the effect of deformation and dynamic recrystallization on grain growth. For example, at the stress magnitudes of our samples that were deformed and then relaxed at 1100°C, ρ is very high, temperature-dependent grain boundary mobility is relatively low, and recovery by dislocation climb is sluggish. The distribution of dislocations in the recrystallized grains appears fairly homogeneous (Figures 8c and 8d), which would promote random ρGBM with little change in the grain size distribution (cf. Platt & Behr, 2011). However, we observed annealed microstructures even in samples with relatively short relaxation intervals, suggesting that strain energy was dissipated (via ρGBM) fairly rapidly. The grain boundaries then migrated toward their centers of curvature (γGBM) and larger grains grew at the expense of smaller grains, resulting in the observed grain size adjustment. The delayed onset of γGBM may help to explain the significant difference between our observed growth rates and those of Karato (1989). However, the similarity of the final grain sizes of 1100°C samples with similar recrystallized grain sizes but different annealing times (w1966, ~1.4 h; w1964, ~14 h) provides evidence that, even after strain energy is dissipated, growth by γGBM is slower than predicted by the Karato (1989) grain growth law.

4.4. Grain size Evolution Following a Reduction in Flow Stress

The olivine piezometer was calibrated using both wet and dry olivine in the stress range of 30-300 MPa. It is based on data from both constant strain rate and rate-stepping experiments, combined with results from single-crystal experiments reported in 1980 by Karato et al. (van der Wal et al., 1993). The recrystallized grain sizes we observe for constant strain rate experiments agree well with the olivine piezometer, even at the higher stress magnitudes made possible by use of the Griggs rig with a molten salt cell. The consistency of our grain sizes with the piezometer over a range of temperatures provides further evidence that the steady state recrystallized grain size is not temperature dependent. Some models for recrystallized grain size explicitly predict temperature dependent piezometric relationships when the activation enthalpy for grain growth is different than that for creep (e.g., Austin & Evans, 2009, and references therein). The observation that our activation enthalpy for grain growth during and subsequent to deformation is similar to that for creep provides a possible explanation for the lack of temperature dependence in the piezometer.

The recrystallized grain sizes observed in samples from rate-stepping experiments are also consistent with the piezometer. van der Wal (1993) investigated grain size evolution after changes in strain rate and found that the grain size adjusted to the new stress within 1.5-3% axial strain. The characteristic strain required for stress-grain size equilibrium has also been reported for other minerals, such as quartz (~3%; Kidder et al., 2016), salt and calcite (3-6% and 20-35%, respectively; Braun et al., 1999, and references therein). With the exception of our sample w2012, the additional strain accumulated during the rate-stepping experiments in this study was 1.3-7.9%, which provides further evidence that the strain required for the recrystallized grain size to keep pace with the piezometer is small for modest changes in stress magnitude. We interpret that the grain size adjustment was facilitated by ρGBM in grains with heterogeneously distributed ρ, and additional recrystallization (from the remaining original porphyroclasts) at the lower stress. Following the large stress drop in our stress relaxation experiments, less than 1% additional strain accumulated, and grain sizes in these samples are no longer consistent with the piezometer. Additional recrystallization would have been very limited; thus, the grain size adjustment can be attributed almost entirely to grain growth.

4.5. Implications for the Persistence of Strain Localization

Exhumed upper mantle shear zones often preserve dynamically recrystallized grain sizes <1 mm with inferred temperatures <1000°C (e.g., van der Wal & Vissers, 1996; Vissers et al., 1997; Warren & Hirth, 2006). High water-content olivine is common in subduction zone settings (e.g., Hirth & Kohlstedt, 1996), and significant water content has been measured in mantle xenoliths and peridotites from orogenic and abyssal settings (e.g., Demouchy et al., 2006; Grant et al., 2007; Warren & Hauri, 2014). Predicted growth curves using our parameters are shown in Figure 12. The shaded regions represent growth from the recrystallized grain sizes predicted by the olivine piezometer based on the stress magnitudes predicted by the wet olivine flow law for a strain rate of 10^{-14} s^{-1} and a range of temperatures (800-1000°C) and confining pressures (2-4 GPa), where higher pressure yields smaller starting grain sizes and slower grain growth for a given temperature. Our results suggest that grain growth of deformed, moderately wet olivine aggregates is much slower than predicted by the existing static grain growth law for wet olivine (Karato, 1989; dashed curves). Also shown in Figure 12 is the range of olivine grain sizes

commonly observed in mantle xenoliths (e.g., Ave Lallemant et al., 1980; Baptiste et al., 2012; Bernard & Behr, 2017; Bernard et al., 2019, and references therein; Mercier, 1980; Tommasi et al., 2008; Zaffarana et al., 2014). Although exact durations of annealing, and dynamically recrystallized grain sizes prior to annealing, are not known for each individual case, for most tectonic settings the eruption age post-dates the timing of the last tectonic event by at least one million years. Our grain growth law is reasonably consistent with the range of observed grain sizes and annealing temperatures for the xenoliths.

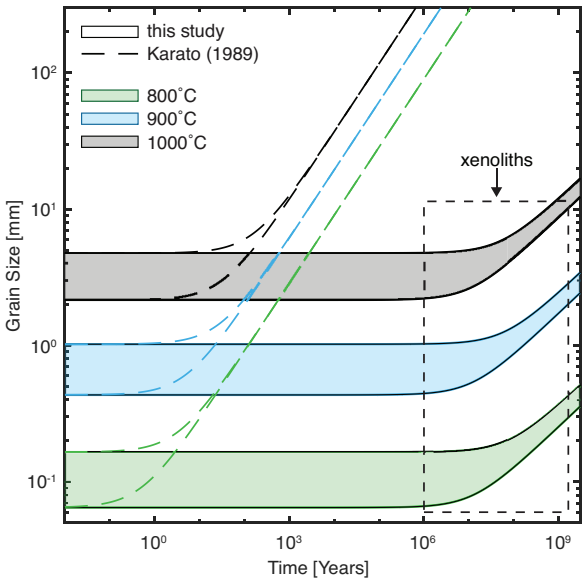

Figure 12. Predicted growth curves using our parameters (shaded curves for a range of starting grain sizes, temperatures, and confining pressures between 2-4 GPa; see text for details) and the existing wet olivine grain growth law (Karato, 1989; dashed curves). The range of grain sizes observed in mantle xenoliths is also shown (dashed box).

5 Conclusions

We performed deformation and grain growth experiments on natural olivine aggregates with moderate water contents. Recrystallized grain sizes in samples quenched after deformation at a constant strain rate agree well with the olivine grain size piezometer (van der Wal et al., 1993). In samples that underwent a reduction in strain rate, grain size adjusted to the piezometer within ~1.3-7.9% strain, suggesting that the critical strain required for stress-grain size equilibrium is small if the stress reduction is small. We quantified post-deformation grain growth rates from stress relaxation experiments which, when extrapolated over geologic time, predict significantly slower growth than that reported for undeformed, wet synthetic olivine (Karato, 1989). We interpret that the grain boundary migration processes that are active during deformation and dynamic recrystallization affect the kinetics of post-deformation grain growth. In samples from our stress relaxation experiments, the development of abundant 120° triple junctions suggests that the reduction of interfacial energy became more important than that of strain energy at some point during the relaxation interval, but growth by γGBM may have been delayed by an interval of random ρGBM. In addition to the effects of grain boundary pinning by secondary phases in naturally deformed mantle rocks (Nes et al., 1985), the results of this study

imply that, because post-deformation grain growth is slow even in moderately wet olivine aggregates, grain size reduction by dynamic recrystallization can play an important role in the persistence of strain localization in the upper mantle.

Acknowledgements

This research was funded by NSF grant 1249737 awarded to W.M. Behr. We thank Shun-ichiro Karato for suggestions related to water content measurement; Daniel Ortega-Arroyo for laboratory assistance; the SEM facility at The University of Texas at Austin's Jackson School of Geosciences for training in connection with EBSD data acquisition; and anonymous reviews that improved the manuscript. Data related to experimental results, paleopiezometry, electron backscatter diffraction, and FTIR can be accessed through the Texas Data Repository at https://data.tdl.org/.

References

Atkinson, H.V. (1988). Theories of normal grain growth in pure single phase systems. *Acta Metallurgica, 36,* 469-491.

Austin, N., & Evans, B. (2007). Paleowattmeters: A scaling relation for dynamically recrystallized grain size. *Geology*, *35(*4), 343-346.

Austin, N., & Evans, B. (2009). The kinetics of microstructural evolution during deformation of calcite. *Journal of Geophysical Research*, *114*, *B09402*, doi:10.1029/2008JB006138

Ave Lallemant, H.G., Mercier, J-C.C., Carter, N.L., & Ross, J.V. (1980). Rheology of the upper mantle: inferences from peridotite xenoliths. *Tectonophysics, 70,* 85-113.

Bachmann, F., Hielscher, R., & Schaeben, H. (2010). Texture analysis with MTEX - free and open source software toolbox. *Solid State Phenomena, 160,* 63–68.

Baptiste, V., Tommasi, A., Demouchy, S. (2012). Deformation and hydration of the lithospheric mantle beneath the Kaapvaal craton, South Africa. *Lithos, 149*, 31-50.

Barnhoorn, A., Bystricky, M., Burlini, L., & Kunze, K. (2004). The role of recrystallisation on the deformation behavior of calcite rocks: large strain torsion experiments on Carrara marble. *Journal of Structural Geology*, *26*, 885-903.

Beck, P.A., Sperry, P.R., & Hsun, H. (1950). The orientation dependence of the rate of grain boundary migration. *Journal of Applied Physics, 21,* 420-425. doi: 10.1063/1.1699676

Behn, M.D., Hirth, G., & Elsenbeck, J.R. (2009). Implications of grain size evolution on the seismic structure of the oceanic upper mantle. *Earth and Planetary Science Letters, 282, 178*-189.

Bercovici, D., & Ricard, Y. (2012). Mechanisms for the generation of plate tectonics by two-phase grain-damage and pinning. *Physics of the Earth and Planetary Interiors, 202-203,* 27-55.

Bercovici, D., & Ricard, Y. (2014). Plate tectonics, damage and inheritance. *Nature, 508,* 513-516. doi:10.1038/nature13072

Bernard, R.E., Behr, W.M. (2017). Fabric heterogeneity in the Mojave lower crust and lithospheric mantle in Southern California. *Journal of Geophysical Research: Solid Earth, 122*, 5000-5025. doi:10.1002/2017JB014280

Bernard, R.E., Behr, W.M., Becker, T.W., Young, D.J. (2019). Relationships between olivine CPO and deformation parameters in naturally deformed rocks and implications for mantle seismic anisotropy. *Geochemistry, Geophysics, Geosystems, 20*, 3469-3494. https://doi.org/10.1029/2019GC008289

Braun, J., Chéry, J., Poliakov, A., Mainprice, D., Vauchez, A., Tomassi, A., & Daignières, M. (1999). A simple parameterization of strain localization in the ductile regime due to grain size reduction: A case study for olivine. *Journal of Geophysical Research, 104, B11,* 25,167-25,181.

Brook, R.J. (1976). Controlled grain growth. In: Wang, F.F.Y. (Ed.), *Ceramic Fabrication Processes: Treatise on Materials Science and Technology*, *9*, 331-364.

Chopra, P.N., & Paterson, M.S. (1984). The role of water in the deformation of dunite. *Journal of Geophysical Research, 89, B9,* 7861-7876.

De Bresser, J.H.P., Ter Heege, J.H., & Spiers, C.J. (2001). Grain size reduction by dynamic recrystallization: can it result in major rheological weakening? *International Journal of Earth Sciences, 90,* 28-45. doi:10.1007/s005310000149

Demouchy, S., Jacobsen, S.D., Gaillard, F., & Stern, C.R. (2006). Rapid magma ascent recorded by water diffusion profiles in mantle olivine. *Geology, 34*(6), 429-432.

Drury, M.R., Vissers, R.L.M, van der Wal, D., & Strating, E.H.H. (1991). Shear localisation in upper mantle peridotites. *Pure Applied Geophysics, 137,* 439-460.

Faul, U.H., & Jackson, I. (2005). The seismological signature of temperature and grain size variations in the upper mantle. *Earth and Planetary Science Letters, 234,* 119-134.

Faul, U.H., & Scott, D. (2006). Grain growth in partially molten olivine aggregates. *Contributions to Mineralogy and Petrology, 151,* 101-111. doi: 10.1007/s00410-005-0048-1

Foley, B.J., Bercovici, D., & Landuyt, W. (2012). The conditions for plate tectonics on super-Earths: inferences from convection models with damage. *Earth and Planetary Science Letters, 331-332,* 281-290.

Freed, A.M., Hirth, G., & Behn, M.D. (2012). Using short-term postseismic displacements to infer the ambient deformation conditions of the upper mantle. *Journal of Geophysical Research, 117, B01409*. doi:10.1029/2011JB008562

Grant, K., Ingrin, J., Lorand, J.P., & Dumas, P. (2007). Water partitioning between mantle minerals from peridotite xenoliths. *Contributions to Mineralogy and Petrology*, *154,* 15-34. doi:10.1007/s00410-006-177-1

Handy, M.R. (1989). Deformation regimes and the rheological evolution of fault zones in the lithosphere: the effects of pressure, temperature, grainsize and time. *Tectonophysics, 163,* 119-152.

Hirth, G., & Kohlstedt, D.L. (1995). Experimental constraints on the dynamics of the partially molten upper mantle 2. Deformation in the dislocation creep regime. *Journal of Geophysical Research, 100, B8,* 15,441-15,449.

Hirth, G., & Kohlstedt, D.L. (1996). Water in the oceanic upper mantle: implications for rheology, melt extraction and the evolution of the lithosphere. *Earth and Planetary Science Letters, 144,* 93-108.

Hirth, G., & Kohlstedt, D.L. (2003). Rheology of the upper mantle and the mantle wedge: a view from the experimentalists. In: J., Eiler (Ed.), *Inside the Subduction Factory, Geophysical Monograph Series* (Vol. 138, pp. 83-105). Washington, DC: American Geophysical Union.

Humphreys, F.J., & Hatherly, M. (1995). *Recrystallization and related annealing phenomena.* Pergamon, Elsevier Science Ltd., 497 p.

Hunter, C.E. (1941). Forsterite olivine deposits of North Carolina and Georgia. Georgia Department of Natural Resources, Division of Mines, Mining, and Geology, *Bulletin Number 47,* 117 p.

Jackson, I., Fitz Gerald, J.D., Faul, U.H., & Tan, B.H. (2002). Grain-size-sensitive seismic wave attenuation in polycrystalline olivine. *Journal of Geophysical Research, 107, B12,* 2360, doi:10.1029/2001JB001225

Karato, S.-I. (1989). Grain growth kinetics in olivine aggregates. *Tectonophysics, 168,* 255-273.

Karato, S.-I., Paterson, M.S., & FitzGerald, J.D. (1986). Rheology of synthetic olivine aggregates: influence of grain size and water. *Journal of Geophysical Research, 91, B8,* 8151-8176.

Karato, S.-i., Toriumi, M., & Fujii, T. (1980). Dynamic recrystallization of olivine single crystals during high-temperature creep. *Geophysical Research Letters, 7*(9), 649-552.

Kidder, S., Hirth, G., Avouac, J.-P., & Behr, W. (2016). The influence of stress history on the grain size and microstructure of experimentally deformed quartzite. *Journal of Structural Geology, 83,* 194-206.

King, D.S.H., Zimmerman, M.E., & Kohlstedt, D.L. (2010). Stress-driven melt segregation in partially molten olivine-rich rocks deformed in torsion. *Journal of Petrology, 51,* 21-42. doi:10.1093/petrology/egp062

Kohlstedt, D.L., Keppler, H., & Rubie, D.C. (1996). Solubility of water in the α, β, and γ phases of $(Mg,Fe)_2SiO_4$. *Contributions to Mineralogy and Petrology, 123,* 345-357.

Korenaga, J. (2013). Initiation and evolution of plate tectonics on Earth: theories and observations. *Annual Review of Earth and Planetary Sciences, 41,* 117-151. doi:10.1146/annurev-earth-050212-124208

Mei, S., & Kohlstedt, D.L. (2000). Influence of water on plastic deformation of olivine aggregates 2. Dislocation creep regime. *Journal of Geophysical Research, 105, B9,* 21,471-21,481.

Mercier, J-C.C. (1980). Magnitude of the continental lithospheric stresses inferred from rheomorphic petrology. *Journal of Geophysical Research, 85,* 6293-6303.

Nes, E., Ryum, N., & Hunderi, O. (1985). On the Zener drag. *Acta Metallurgica, 33,* 11-22.

Newman, J., & Drury, M.R. (2010). Control of shear zone location and thickness by initial grain size variations in upper mantle peridotites. *Journal of Structural Geology, 32,* 832-842.

Newman, J., Lamb, W.M., Drury, M.R., & Vissers, R.L.M. (1999). Deformation processes in a peridotite shear zone: reaction-softening by an H_2O-deficient, continuous net transfer reaction. *Tectonophysics, 303,* 193-222.

Nichols, S.J., & Mackwell, S.J. (1991). Grain growth in porous olivine aggregates. *Physics and Chemistry of Minerals, 18,* 269-278.

Ohuchi, T., & Nakamura, M. (2007). Grain growth in the forsterite-diopside system. *Physics of the Earth and Planetary Interiors, 160,* 1-21.

Pantleon, W. (2008). Resolving geometrically necessary dislocation content by conventional electron backscattering diffraction. *Scripta Materialia, 58,* 994-997.

Paterson, M.S. (1982). The determination of hydroxyl by infrared absorption in quartz, silicate glasses and similar materials. *Bulletin of Mineralogy, 105,* 20-29.

Platt, J.P., & Behr, W.M. (2011). Grainsize evolution in ductile shear zones: implications for strain localization and the strength of the lithosphere. *Journal of Structural Geology, 33,* 537-550.

Poirier, J.P. (1980). Shear localization and shear instability in materials in the ductile field. *Journal of Structural Geology, 2,* 135-142.

Proctor, B., & Hirth, G. (2015). Role of pore fluid pressure on transient strength changes and fabric development during serpentine dehydration at mantle conditions: Implications for subduction-zone seismicity. *Earth and Planetary Science Letters, 421,* 1-12.

Rozel, A., Ricard, Y., & Bercovici, D. (2011). A thermodynamically self-consistent damage equation for grain size evolution during dynamic recrystallization. *Geophysical Journal International, 184,* 719-728. doi: 10.1111/j.1365-246X.2010.04875.x

Rubie, D.C. (1983). Reaction-enhanced ductility: the role of solid-solid univariant reactions in deformation of the crust and mantle. *Tectonophysics, 96,* 331-352.

Rutter, E.H. (1995). Experimental study of the influence of stress, temperature, and strain on the dynamic recrystallization of Carrara marble. *Journal of Geophysical Research*, *100*(B12), 24,651-24,663.

Schmid, S.M., Paterson, M.S., & Boland, J.N. (1980). High temperature flow and dynamic recrystallization in Carrara marble. *Tectonophysics*, *65*, 245-280.

Skemer, P., Sundberg, M., Hirth, G., Cooper, R. (2011). Torsion experiments on coarse-grained dunite: implications for microstructural evolution when diffusion creep is suppressed. *Geological Society, London, Special Publications*, *360*, 211-223.

Stipp, M., & Tullis, J. (2003). The recrystallized grain size piezometer for quartz. *Geophysical Research Letters*, *30*(21,2088), doi:10.1029/2003GL018444

Tommasi, A., Vauchez, A., Ionov, D.A. (2008). Deformation, static recrystallization, and reactive melt transport in shallow subcontinental mantle xenoliths (Tok Cenozoic volcanic field, SE Siberia). *Earth and Planetary Science Letters, 272*, 65-77.

Tullis, T.E., & Tullis, J. (1986). Experimental rock deformation techniques. In: B.E. Hobbs, B.E., & H.C. Heard (Eds.), *Mineral and Rock Deformation: Laboratory Studies: The Paterson Volume* (pp. 297-324). Washington, DC: American Geophysical Union.

van der Wal, D. (1993). *Deformation processes in mantle peridotites with emphasis on the Ronda peridotite of SW Spain* (Doctoral dissertation). Netherlands: Geologica Ultraiectina, 181 p.

van der Wal, D., & Vissers, R.L.M. (1996). Structural petrology of the Ronda Peridotite, SW Spain: deformation history. *Journal of Petrology, 37*(1), 23-43.

van der Wal, D., Chopra, P., Drury, M, & Fitz Gerald, J. (1993). Relationships between dynamically recrystallized grain size and deformation conditions in experimentally deformed olivine rocks. *Geophysical Research Letters, 20*(14), 1479-1482.

Vissers, R.L.M., Drury, M.R., Newman, J., & Fliervoet, T.F. (1997). Mylonitic deformation in upper mantle peridotites of the North Pyrenean Zone (France): implications for strength and strain localization in the lithosphere. *Tectonophysics, 279,* 303-325.

Warren, J.M., & Hauri, E.H. (2014). Pyroxenes as tracers of mantle water variations. *Journal of Geophysical Research: Solid Earth, 119,* 1851-1881, doi:10.100/2013JB010328

Warren, J.M., & Hirth, G. (2006). Grain size sensitive deformation mechanisms in naturally deformed peridotites. *Earth and Planetary Science Letters, 248,* 438-450.

White, S.H., & Knipe, R.J. (1978). Transformation- and reaction-enhanced ductility in rocks. *Journal of the Geological Society*, London, *135,* 513-516.

White, S.H., Burrows, S.E., Carreras, J., Shaw, N.D., & Humphreys, F.J. (1980). On mylonites in ductile shear zones. *Journal of Structural Geology, 2,* 175-187.

Zaffarana, C., Tommasi, A., Vauchez, A., Grégoire, M. (2014). Microstructures and seismic properties of south Patagonian mantle xenoliths (Gobernador Gregores and Pali Aike). *Tectonophysics, 621*, 175-197.

Zhao, Y-H., Ginsberg, S.B., Kohlstedt, D.L. (2004). Solubility of hydrogen in olivine: dependence on temperature and iron content. *Contributions to Mineralogy and Petrology*, *147*, 155-161.

Zhu, W., Gaetani, G.A., Fusseis, F., Montési, L.G.J., & De Carlo, F. (2011). Microtomography of partially molten rocks: three-dimensional melt distribution in mantle peridotite. *Science, 332,* 88-91.

This manuscript is a non-peer reviewed EarthArXiv preprint. It is under review in *Journal of Geophysical Research: Solid Earth*.

Supporting Information for

Rates of olivine grain growth during dynamic recrystallization and post-deformation annealing

P.A. Speciale[1*], W.M. Behr[1,2], G. Hirth[3], and L. Tokle[2,3]

[1]Department of Geological Sciences, Jackson School of Geosciences, The University of Texas at Austin, Austin, Texas, USA. [2]Geological Institute, Department of Earth Sciences, ETH Zürich (Swizz Federal Institute of Technology), Zürich, Switzerland. [3]Department of Earth, Environmental, and Planetary Sciences, Brown University, Providence, Rhode Island, USA.

Contents of this file

Introduction

This supporting information contains data regarding measurement of hydroxyl concentrations in the starting material and a deformed sample in this study, measured with FTIR (Figure S1), grain size histograms plotted as frequency vs. Log10(grain size in μm) in Figure S2, and plots of electron microprobe analyses of CaO and Al_2O_3 content in several samples (Figure S3).

Text S1. Hydroxyl concentrations

We quantified hydroxyl concentrations in the starting material and a deformed sample using Fourier transform infrared (FTIR) spectroscopy (Figure S1). Olivine grains from each sample were embedded in CrystalbondTM and doubly polished to a thickness of ~360 µm and ~300 µm, respectively. The CrystalbondTM was dissolved in acetone and the grains were washed with ethanol followed by distilled water. Vertical thickness was measured using a pin micrometer. We averaged several measurements made on each grain, all of which differed by <10 µm. Spectra were acquired using a ThermoElectron Nicolet 6700 spectrometer and Continuµm IR microscope at the University of Texas at Austin, at a resolution of 4 cm–1 and aperture size of 50 µm. IR spectra were collected at 3-4 spots for each sample. Grains were oriented such that the beam was perpendicular to (010). We applied the calibration of Paterson (1982):

$$C_{OH} = \frac{\varphi}{150\xi}\int \frac{k(v)}{3780 - v}dv$$

where C_{OH} is the hydroxyl concentration, ξ is the orientation factor (½ for unpolarized IR incident on the (010) plane), k(v) is the absorption coefficient, and v is the wave number. The density factor φ is assumed to be 4.39×10^4 ppm H/Si (Kohlstedt et al., 1996). After baseline correction, spectra were integrated between 3000 to 3780 cm^{-1}. The absorption coefficients were normalized to a wafer thickness of 1 cm. Average hydroxyl concentration is C_{OH} ~350 ppm H/Si in the starting material, and C_{OH} ~900 ppm H/Si in the deformed sample. We interpret that the relatively high C_{OH} in the deformed sample represents a maximum water content, as the spectra are broad rather than having sharp peaks characteristic of OH stretching caused by water dissolved in the crystal structure. The reason for the broad spectra in the deformed sample (w2018) is unclear, but we speculate that the beam may have encountered subgrain boundaries. The broad spectra result in large uncertainties, so we estimate water content to be C_{OH} = 600 ± 300 ppm H/Si.

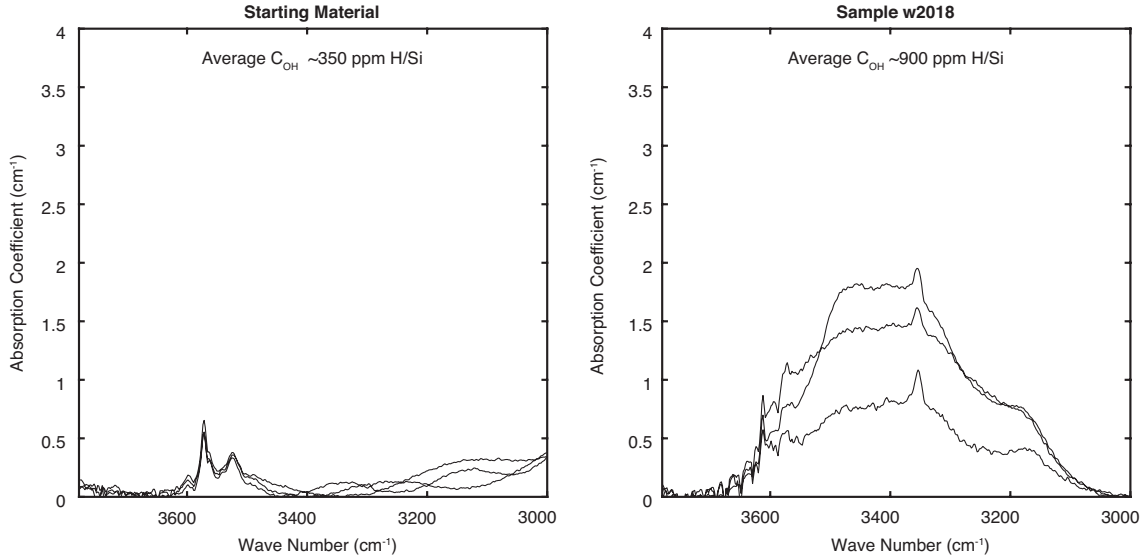

Figure S1. FTIR spectra.

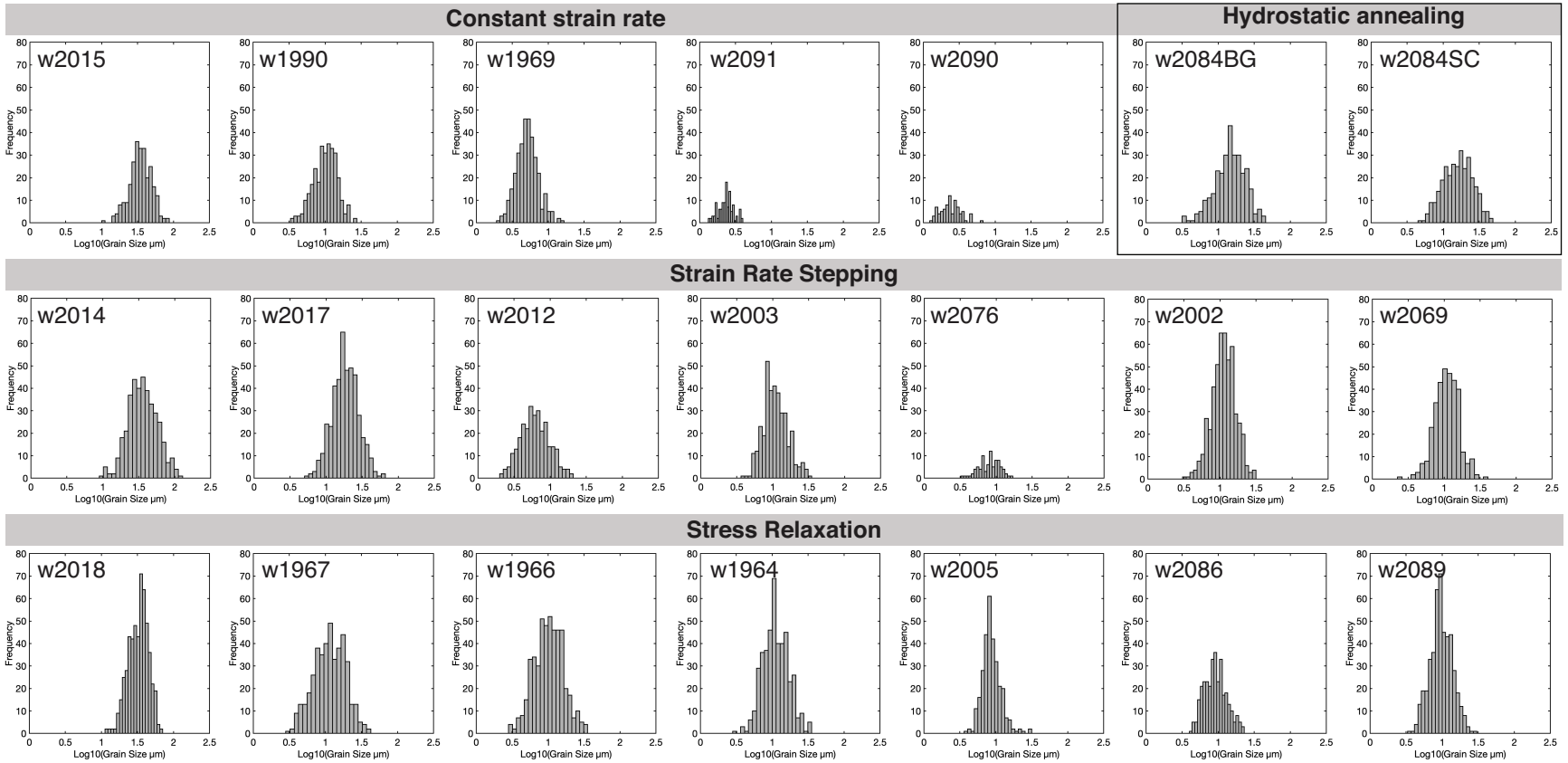

Figure S2. Grain size histograms.
Frequency vs. Log10(Grain Size in µm).

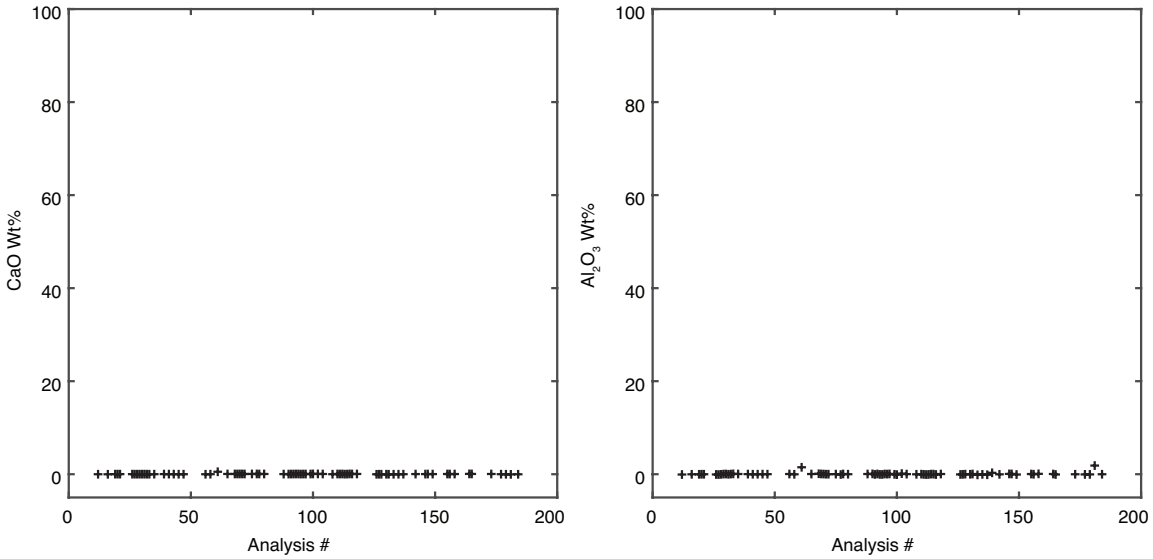

Figure S3. Electron microprobe analysis of CaO (<0.06 wt%) and Al_2O_3 (<0.15 wt%) in several samples from this study.